Photometric Analysis of Asteroids in the Phocaea Region

Xu, Xiaoyun; Wang, Xiaobing; Muinonen, Karri; Gu, Shenghong; Penttilä, Antti ...

2025-07
American Astronomical Society
http://hdl.handle.net/10138/600037
Xu, X, Wang, X, Muinonen, K, Gu, S, Penttilä, A, Xu, F, Sun, L, Huang, J, Zhang, P & Wang, A 2025, 'Photometric Analysis of Asteroids in the Phocaea Region', Astronomical Journal, vol. 170, no. 1, 35. https://doi.org/10.3847/1538-3881/add3f4

The Astronomical Journal, 170:35 (15pp), 2025 July https://doi.org/10.3847/1538-3881/add3f4

Photometric Analysis of Asteroids in the Phocaea Region

Xiaoyun Xu[1,2,7], Xiaobing Wang[1,2,3,7], Karri Muinonen[4], Shenghong Gu[1,2,3], Antti Penttilä[4], Fukun Xu[1,2,3], Leilei Sun[1,2,3], Jing Huang[1,2], Pengfei Zhang[5], and Ao Wang[6]
[1] Yunnan Observatories, Chinese Academy of Sciences, Kunming 650216, People's Republic of China; wangxb@ynao.ac.cn
[2] University of Chinese Academy of Sciences, Beijing 100049, People's Republic of China
[3] Key Laboratory for the Structure and Evolution of Celestial Objects, Chinese Academy of Sciences, Kunming 650216, People's Republic of China
[4] Department of Physics, P.O. box 64, FI-00014, University of Helsinki, Finland
[5] Center for Lunar and Planetary Sciences, Institute of Geochemistry, Chinese Academy of Sciences, Guiyang, People's Republic of China
[6] Department of Physics, Yuxi Normal University, Yuxi 653100, People's Republic of China
Received 2025 February 17; revised 2025 April 28; accepted 2025 May 1; published 2025 June 12

Abstract

The Phocaea asteroid family, one of the large ancient families located in the inner main belt, may be the sources of near-Earth asteroids (NEAs) due to the nearby 3:1 mean motion resonance with Jupiter, the $\nu 6$ secular resonance, and the Yarkovsky and Yarkovsky–O'Keefe–Radzievskii–Paddack (YORP) effects. Thus, understanding the influence of the Yarkovsky and YORP effects on the Phocaea family is one of the keys to figuring out the source of NEAs. However, the physical properties of most of the Phocaea family members are unknown at present. We perform a photometric analysis for 44 asteroids in the Phocaea region using photometric data obtained by ground-based and space-based telescopes (i.e., the Transiting Exoplanet Survey Satellite and Gaia). Based on the derived physical properties, we find significant footprints of the Yarkovsky and YORP effects on the Phocaea family members. Selecting five asteroids nearby the inside boundary of the V shape in the absolute-magnitude semimajor-axis (H, a) space, we estimate their densities considering their migration in semimajor-axis arises from the Yarkovsky effect. The bulk density of (852) Wladilena (3.54 g cm^{-3}) suggests a link to the H chondrite meteorites. Incorporating the grain density of the H chondrites, we estimate the macroporosities of the asteroids (290) Bruna, (1164) Kobolda, and (587) Hypsipyle, respectively, as 41%, 47%, and 65%, implying rubble pile structures. Considering the H chondrites link to asteroid (25) Phocaea, we suggest the parent body of the Phocaea family has been composed of H chondrite like material and the Phocaea family may be one of the sources of H chondrite meteorites.

Unified Astronomy Thesaurus concepts: Asteroids (72); Chondrites (228); Photometry (1234); Sky surveys (1464)

1. Introduction

Asteroids with similar orbits, i.e., proper semimajor axes, eccentricities, and inclinations, can constitute a dynamical family. Such families, also called asteroid families, are thought to have their origins in catastrophic collisions of larger parent bodies. Family members, fragments of such collision events, have been subject to both gravitational and nongravitational effects, such as the Yarkovsky and Yarkovsky–O'Keefe–Radzievskii–Paddack (YORP) effects. Of course, they have also experienced space weathering, solar heating, and maybe subsequent collisions. The physical properties and orbits of these asteroids have been shaped by the above-mentioned effects (J. R. Masiero et al. 2015). To an extent, asteroid families are valuable laboratories for humans to study planetary-scale impact physics, which could provide us with important insight into the task of planetary defense, as well as help us to figure out the origin and evolution of asteroids (B. Novaković et al. 2022).

We are interested in the Phocaea dynamical family for several reasons. First, it is one of the largest ancient asteroid families formed by a collisional outbreak (J. M. Carvano et al. 2001). Second, its special location in the solar system, near three resonances (the 7:2 and 3:1 mean motion resonances with Jupiter and the υ_6 secular resonance), suggests that it can be a source of near-Earth asteroids (NEAs, W. F. Bottke et al. 2000; M. Granvik et al. 2018; M. Marsset et al. 2022). Third, the Phocaea dynamical region will be covered by the survey of the Chinese Space Station Telescope (CSST), by which multiple band photometric data for asteroids of apparent magnitude brighter than 26 mag and spectroscopic data of wavelength range from 0.255 to 1.0 μm for asteroids brighter than 23 mag can be obtained (H. Zhan 2021). Asteroid (25) Phocaea is the largest member of the Phocaea family, also one of the largest known S-type asteroids the inner main belt of asteroids. At present, there are 5796 members of the Phocaea family, according to information on the Asteroid Families Portal.[8] Actually, discussing Phocaea region is preferable (an orbital region of semimajor axes ranging from 2.2 to 2.5 au, eccentricities between 0.1 and 0.3, and inclinations from 17° to 27°), because the Tamara family, composed of dark asteroids, is also located in this region. About 87% of the Phocaea family members are fainter than 15 mag. Due to observational constraints, members with known physical properties are rare. J. M. Carvano et al. (2001) first determined the spectral types of 31 asteroids in the Phocaea region, and found that 24 members are S-type, three are C-type, three are X-type, and one is D-type. V. Carruba (2009) analyzed the spectra of 50

[7] These authors contributed to the work equally and should be regarded as co-first authors.

[8] http://asteroids.matf.bg.ac.rs/fam/

asteroids in the Phocaea region: 36 are identified as S-type and four as C-type, with 10 belonging to other types. Most of the information on the members of the Phocaea region comes from the observations of the Near-Earth Object Wide-Field Infrared Survey Explorer (NEOWISE)[9] mission, by which the diameters and albedos of 1307 asteroids in the Phocaea region are determined. Among 1307 asteroids, 85% asteroids have diameters smaller than 5 km and 62% have an S-type geometric albedo (ranging from 0.15 to 0.4). The percentage of asteroids with S-type albedo is consistent with previous studies (J. M. Carvano et al. 2001; V. Carruba 2009) showing that the Phocaea region is predominantly composed of S-type asteroids. Adding albedo information of asteroids, B. Novaković et al. (2017) identified a new asteroid family consisting of 226 low-albedo asteroids in the Phocaea region, which implies a more complex family structure in the region. For the age of the Phocaea family, V. Carruba (2009) provided an upper limit of 2200 Myr using the method of D. Vokrouhlický et al. (2006). A. Milani et al. (2017) determined its age as 1187 ± 319 Myr by fitting the inner side of the so-called V shape in $(1/D, a)$ plane (D and a are the diameter and semimajor axis).

As for the spin and shape of the members of Phocaea family, V. Carruba (2009) determined rotation periods for 18 asteroids. With eight out of the 18 asteroids being slow rotators, the excess of slow rotators was considered to be a result of the YORP effect. J. Hanuš et al. (2013a) have carried out photometric inversion for 14 members of the Phocaea family, finding significantly more retrograde than prograde rotators. Obviously, to understand the origin and evolution of the asteroids in the Phocaea region, it is necessary to derive basic physical properties such as size, shape, spin, composition, and even density for a larger number of asteroids in the region.

Nowadays, time-domain space-based and ground-based surveys are running or being prepared, providing us opportunities to extend the physical properties of asteroids and to uncover puzzles of the origin and evolution of individual asteroids, asteroid families, and even the entire asteroid main belt. For example, Gaia DR3 provided calibrated G-band sparse photometric data for more than 150,000 asteroids with multiple observed geometry and spectroscopic data for 60,518 asteroids (P. Tanga et al. 2023). Based on Gaia DR3 photometric data and ground-based photometric data, A. Cellino et al. (2024) determined the rotation periods, pole orientations, shapes, and photometric slopes for over 22,000 asteroids. J. Martikainen et al. (2021) did photometric inversion for 491 asteroids with the Gaia DR2 data and ground-based data from the Database of Asteroid Models from Inversion Techniques (DAMIT). The Transiting Exoplanet Survey Satellite (TESS) mission, a time-domain survey dedicated to searching for new transit exoplanets, provides dense light curves of 9912 asteroids (A. Pál et al. 2020). The Yunnan–Hong Kong Wide Field Photometric Survey (YNHK), a ground-based time-domain survey also dedicated for new transiting exoplanets, has offered dense light curves for 546 asteroids (S. Gu et al. 2022; X. Xu et al. 2023).

By performing light-curve inversion, in the present work we determine the physical parameters of 44 asteroids in the Phocaea region with photometric data from Gaia DR3, TESS data release, YNHK survey, and the DAMIT database. It is worth mentioning that the absolute magnitudes and photometric slopes of the 44 asteroids are determined because the calibrated magnitudes (e.g., Gaia DR3, TESS data release, and YNHK data) of selected asteroids are involved. Based on the derived spin parameters of 44 asteroids, we may have the opportunity to investigate the influence of the YORP and Yarkovsky effects on the Phocaea family.

This paper is organized as follows. Section 2 gives the information on the photometric observations and data reduction for 44 selected asteroids in the Phocaea region. The photometric inversion methods used in this work are shown in Section 3. The photometric inversion results of 44 asteroids and related discussions are presented in Section 4. Finally, a summary is given in the last section.

2. Photometric Data

Photometry is the most economical and efficient way to determine the physical properties of asteroids. The value of brightness of an asteroid at a certain time and the shape of its light curve (brightnesses at different time) are related to the asteroid's physical properties (i.e., size, shape, spin parameters, and surface scattering parameters) and observational geometries. This means that from both dense light curves and sparse calibrated brightnesses of asteroids, we can extract their related physical parameters, as shown by J. Martikainen et al. (2021). In this work, we performed light-curve inversion for 44 selected asteroids using their dense light curves and sparse photometric data, some of which are obtained by ground-based and space-based surveys. The sparse photometric data of 44 involved asteroids used in this work comes from Gaia DR3, which are calibrated G-band magnitudes covering phase angles ranging from 10° to 40° for main-belt asteroids (P. Tanga et al. 2023). The dense photometric data of the 44 involved asteroids come from data release of the TESS survey, the YNHK survey, the DAMIT database (J. Durech et al. 2010), and the Asteroid Lightcurve Data Exchange Format (ALCDEF) Database of the Minor Planet Center (B. D. Warner et al. 2009).

The YNHK survey employs a Centurion 18-inch telescope attached with a clear filter at the Lijiang station of Yunnan Observatories and is a time-domain survey dedicated to the search for new exoplanets. The YNHK survey has been run more than 7 yr by our team (S. Gu et al. 2022). To search for new transit exoplanets from the YNHK survey, S. Gu et al. (2022) built a data reduction pipeline which contains four parts: basic image processing, astrometry calibration and crossmatch with a certain catalog, photometric measurement, and read noise correction. In order to extract dense light curves of asteroids from the YNHK survey, we developed a special subpipeline using machine learning techniques (X. Xu et al. 2023). With our special subpipeline, asteroids are identified with their celestial coordinates and velocities. Then, the data reduction procedure of asteroids in the YNHK survey is the same as that of stellar objects when the coordinates of asteroids identified by our special subpipeline are added into the input catalog, which is customized according to the specific scientific goals. The detailed information can refer to papers (S. Gu et al. 2022; X. Xu et al. 2023). A recently update for our pipeline is that the Gaia DR3 catalog (Gaia Data Release 3) is applied in the astrometric and photometric calibrations.

The TESS survey provides calibrated dense light curves of 9912 asteroids at a cadence of 30 minutes (A. Pál et al. 2020). Compared to ground-based observations, the TESS survey has

[9] https://sbn.psi.edu/pds/resource/neowisediam.html

the merit of continuous 24 hr observation, which is important for physical studies of asteroids with a long rotational period. Before the photometric analysis, the calibrated TESS magnitudes m_T are converted into the Gaia G-band magnitudes m_G with the aid of the transformation relationships provided by K. G. Stassun et al. (2018); M. Riello et al. (2021):

$$m_G = m_T + 0.2991 - 0.0057^*(g - i) + 1.298^*(r - i), \quad (1)$$

where the color indices $(g - i)$ and $(r - i)$ of the asteroids come from the database of the Sloan Digital Sky Survey (Z. Ivezic et al. 2020).

The dense light curves of our targets are from the ALCDEF and DAMIT databases. The ALCDEF database contains photometric data for more than 24,000 asteroids. The light curves of 44 selected asteroids from the ALCDEF database have a quality code $U \geqslant 2$.

For all photometric data included, the light travel times of asteroids are corrected for and the apparent magnitudes of the asteroids are converted into reduced magnitudes, i.e., the values at 1 au distances from the Sun and the observers.

In the photometric analysis for 44 asteroids in the Phocaea region, 453 dense light curves and 1105 sparse photometric data from the previously described data sets are included. In detail, 330 dense relative light curves of 37 asteroids, observed by ground-based telescopes, were downloaded from the ALCDEF and DAMIT databases. These data have time intervals ranging from one minute to several minutes. The 121 light curves of nine asteroids from the TESS survey and two dense light curves of the asteroid (1626) Sadeya come from the YHNK survey. Sparse photometric data of asteroids mainly come from Gaia DR3, there are at least 12 data points at more than three different phase angles for each asteroid.

3. Photometric Inversion

To invert the physical properties of the Phocaea family members from the photometric data, we perform Bayesian light curve inversion developed by K. Muinonen et al. (2020, 2022). The disk-integrated brightness of an asteroid at a certain observational geometry is derived by the sum of radiation reflected from the illuminated and visible surface area of the asteroid. Thus, the brightness model of the asteroid in the Bayesian light-curve inversion method involves a convex shape represented with truncated spherical harmonics, the Lommel–Seeliger scattering model, and the H, G_1, G_2 phase function. Setting a triangulation for the unit sphere, the observed brightness of an asteroid at any time can be calculated as the following formal sum,

$$\begin{aligned} L(E, E_0, \alpha) &= \Sigma S(\mu_i, \mu_{0,i}) G(\vartheta_i, \psi_i)\sigma_i, \\ S(\mu, \mu_0) &= 2p\frac{\Phi(\alpha)}{\Phi_{LS}(\alpha)}\frac{1}{\mu + \mu_0}, \\ \mu &= E \cdot n, \ \mu_0 = E_0 \cdot n, \end{aligned} \quad (2)$$

where E, E_0 represent the directions of the observer and source and $G(\vartheta_i, \psi_i)\sigma_i$ denotes the size of the facet with the unit normal vector $n(\vartheta_i, \psi_i)$. The Gaussian surface density function $G(\vartheta, \psi)$ is approximated with truncated spherical harmonics in the practical computation. $\Phi_{LS}(\alpha)$ denotes the Lommel–Seeliger phase function (see Equation (6) in K. Muinonen et al. 2020) and $\Phi(\alpha)$ is a linear phase function (see Equation (10) in K. Muinonen et al. 2022).

Considering that the asteroid spins about its axis of maximum inertia, the unknown parameters in the brightness of the asteroid can be $\boldsymbol{P} = (T, \lambda_p, \beta_p, \varphi_0, s_{00},\ldots,s_{l_{\max}l_{\max}}, m_{20}, \beta_s)$. In detail, T, λ_p, β_p, φ_0 are the spin parameters of the asteroid. If one sets $l_{\min} = 0$ and $l_{\max} = 6$, there will be 49 spherical harmonics coefficients or, say, shape parameters $s_{00},\ldots,s_{l_{\max}l_{\max}}$. The phase function parameter β_s and m_{20} are involved because of application to absolute Gaia data. The determination procedure for the unknown parameters with the Bayesian inversion actually contains the least-squares fitting and the Markov Chain Monte Carlo (MCMC) analysis parts. The chi-square sum is computed with a weighting scheme determined by the quality of data and the duration and time resolution of the observations,

$$\begin{aligned} \chi^2(\boldsymbol{P}) \approx \sum_{i=1}^{4}\sum_{k=1}^{K_i} &\frac{(2.5\log_{10} \quad \mathrm{e})^2}{\sigma_{\epsilon,ik}^2} \\ &\times \sum_{j=1}^{N_{ik}}\left[\frac{L_{\mathrm{obs},ikj} - L_{ikj}(\boldsymbol{P})\ 10^{0.4\Delta M_{ik0}(\boldsymbol{P})}}{L_{obs,ikj}}\right]^2, \\ \sigma_{\epsilon,ik} = \sqrt{\frac{N_{ik}}{N_{ik,\mathrm{eff}}}}&\max(\sigma_{0,ik}, \sigma_{pr,ik}), \end{aligned} \quad (3)$$

where N_{ik} and $\sigma_{\epsilon,ik}$ are the number of observations and the weight of the ik-th light curve, $L_{\mathrm{obs},ikj}$ and $L_{ikj}(\boldsymbol{P})$ are the observed and computed brightnesses, and $\Delta M_{ik0}(\boldsymbol{P})$ is the averaged difference between observed and computed magnitudes. The index i in the above formula represents the characteristic of each light curve, $i = 1, 2, 3, 4$ refer to dense relative, sparse relative, dense absolute, and sparse absolute light curve, respectively. The dense and sparse light curves are identified according to the sampling rates of the light curves in time. $N_{ik,\mathrm{eff}}$ is the so-called efficient number of observations in the light curve. For relative light curve. $N_{ik,\mathrm{eff}}$ is estimated by comparing the mean sampling time interval of the light curve to that of the most sparse relative light curve. For absolute light curves, $N_{ik,\mathrm{eff}}$ is set to unity. The initial values of $\sigma_{0,ik}$ are set as the standard deviation of the spline fitting to the raw data. Then, they are related to the rms of the O–C residuals between the observed and computed brightnesses. $\sigma_{pr,ik}$ is a prior threshold of uncertainty, set to 0.005 mag for dense light curves and 0.02 mag for the Gaia data.

First, we apply the Levenberg-Marquardt algorithm to find the least-squares solution for the unknown parameters. During the least-squares fitting procedure, the involved parameters $\boldsymbol{P}$ and $\sigma_{\epsilon,ik}$ are refined iteratively until they converge.

Second, the virtual observation MCMC analysis for the photometric data of 44 asteroids is done using the Metropolis-Hastings algorithm. During the virtual observation MCMC procedure, a set of virtual observations M_v is generated from the original observations M_{obs} by adding additional Gaussian random quantities of given uncertainties ν and a covariance matrix Λ. A set of virtual least-squares solutions of unknown parameters are derived from the virtual observation sets. Then, a random-walk MCMC sampling is performed from the symmetric proposal probability density function (pdf) composed of the virtual least-squares solution of parameters. More detailed mathematical description can be found in K. Muinonen et al. (2020). Based on a posteriori pdfs of involved

parameters, the best parameter values and their uncertainties are obtained.

Additionally, we estimated the G-band absolute magnitudes, H_G, and phase function parameters G_1, G_2 of 44 asteroids with J. Martikainen et al.'s (2021) method. In practice, these parameters are derived by fitting the phase curves of 44 asteroids at reference geometry (equivalent an equatorial illumination and observation) with the help of convex shape solutions derived in the MCMC procedure. Because only the Gaia data are absolute photometry in the analysis, the slopes $\beta_{\rm ref}$ and H_G of the mean-magnitude reference phase curve are estimated (K. Muinonen et al. 2022).

In the least-squares fitting, the initial rotation periods of 44 asteroids are retrieved from the Asteroid Lightcurve Database (LCDB,[10] B. D. Warner et al. 2009) or DAMIT database. The initial rotational phase φ_0 is typically set to zero at a given epoch t_0, which generally is the brightness minimum. The initial pole orientations of 42 members were obtained from the DAMIT database. The asteroids (8356) Wadhwa and (23552) 1994 NB do not have prior estimates of their pole orientation and shape. For these two asteroids, a systematic scan with 10° mesh over the unit sphere is performed to find their possible pole solutions with the least-squares method. Once the initial values of the spin parameters are determined, the optimization algorithm is applied to iteratively refine the shape and phase function parameters.

4. Results and Discussion

4.1. The Spin Parameters and Shapes

Applying the Bayesian light curve inversion method, we analyze the photometric data of 44 asteroids in the Phocaea region, and obtain their convex shape, spin parameters, and phase function parameter. The best values for the spin parameters are presented in Appendix A (Table 2), the photometric slope $\beta_{\rm ref}$ with their uncertainties are presented in Appendix A (Table 3). Using the Minkowski problem solver, the convex shape of the best-fit solution has been reconstructed (see Figure 5 in Appendix C).

Among the involved asteroids, we obtained the unique pole solution for 40 asteroids in this photometric inversion, while for four other asteroids, (587) Hypsipyle, (6510) Tarry, (23552) 1994 NB and (29729) 1999 BY 1, we could not rule out their mirror pole solutions (a pair of pole solutions at similar latitudes but with longitudes differing by 180°). This ambiguity may arise from the limitation of the observational geometry of the photometric data used. In practice, we generally tested their possible mirror pole for all involved asteroids, and then compared the fitting situations for the pair of mirrored pole solutions. Finally, we selected the admissible pole solution for each asteroid by considering the fitting situation of modeled brightnesses to observed ones, especially to the Gaia data. Statistically speaking, we determined the basic physical parameters of two asteroids for the first time, and derived the more precise parameters for other 42 asteroids. For example, the uncertainties of rotation period for 44 asteroids range from 10^{-7} to 10^{-5} hr, and the uncertainties of pole orientations in both ecliptic longitude and latitude are less 5°.

[10] https://minplanobs.org/mpinfo/php/lcdb.php

As examples, the light curve inversion results are shown for four asteroids: (1626) Sadeya, (6560) Pravdo, (8356) Wadhwa, and (23552) 1994 NB.

(1626) Sadeya

Several groups have carried out physical studies for (1626) Sadeya, deriving different pole solutions. J. Ďurech et al. (2020) derived a pole solution of (250°, −37°), with a rotation period of 3.42015 hr. R. D. Stephens & B. D. Warner's (2021) study suggested a pole solution of (152°, −9°) of a rotation period of 3.421367 hr. In this analysis, 14 dense light curves of Sadeya and 16 calibrated Gaia data are involved. These dense light curves are obtained by ground-based telescopes at five apparitions: 2007, 2009, 2014, 2018, and 2020, with the phase angle of the Gaia data ranging from 17° to 25°. We obtained the best pole solution of ($251\overset{\circ}{.}7 \pm 1\overset{\circ}{.}5$, $-43\overset{\circ}{.}2 \pm 1\overset{\circ}{.}4$) with a period of 3.4201645 ± 0.0000005 hr. Figure 4(a) in Appendix B shows example photometric data (blue circles) for Sadeya (left: a dense light curve, right: Gaia data) together with the model points (red symbols) computed by using the chosen admissible pole solution represented. The observed-minus-computed (O–C) residuals are shown in the bottom panel of Figure 4(a). For the chosen pole solution, the χ^2 value is 28.7 and the rms value of Gaia data is 0.0024 mag. For the mirror pole solution ($65\overset{\circ}{.}5 \pm 1\overset{\circ}{.}1$, $19\overset{\circ}{.}8 \pm 1\overset{\circ}{.}7$), χ^2-value is 30.2 and the rms value of Gaia data is higher at 0.0127 mag for the Gaia data. Thus, we consider the former pole as the preferred pole solution.

(6560) Pravdo

Physical studies for (6560) Pravdo have been restricted because of the limited availability of photometric data. Using sparse data from the ATLAS survey, J. Ďurech et al. (2020) roughly estimated the ecliptic latitude of the pole as 56° with an uncertainty of 18°. Recently, J. Ďurech & J. Hanuš (2023) determined its shape and pole parameters using Gaia data. The new derived pole orientation is (174°, 48°) with a rotation period of 19.1981 hr. Using 17 dense light curves obtained by TESS and 33 Gaia data points, we analyze the physical parameters of (6560) Pravdo. The dense light curves from TESS of a 30 minutes cadence are obtained consequently within 14 days. The 33 Gaia points cover phase angles from 15° to 29°. We obtained the best values for spin parameters of ($174\overset{\circ}{.}2 \pm 1\overset{\circ}{.}0$, $51\overset{\circ}{.}4 \pm 2\overset{\circ}{.}3$) with a rotation period of 19.1980260 ± 0.0000201 hr, close to the results reported by J. Ďurech & J. Hanuš (2023). The χ^2-value of the best pole solution is 47.1, and the rms value of the Gaia data is 0.0071 mag. In comparison, the mirror pole solution of ($348\overset{\circ}{.}8$, $88\overset{\circ}{.}7$) gives the rms value of 0.0257 mag for Gaia data, which is significantly larger than that for the best pole solution, so it is rejected. Figure 4(b) in Appendix B presents example photometric data with computed values for (6560) Pravdo. The shape of the light curves for Pravdo shows a regular double-peaked sinusoidal structure with a high amplitude close to 0.75 mag. Consequently, an elongated shape suggesting binary characteristics is derived (see Figure 5 in Appendix C).

(8356) Wadhwa

The physical parameters of (8356) Wadhwa are here derived for the first time by us. In the present photometric analysis, 11 dense light curves and 28 Gaia data points of (8356) Wadhwa are used. The dense light curves, observed at three different apparitions, are collected from R. K. Buchheim (2009) and the ALCDEF database. We obtained the best-fit pole solution of

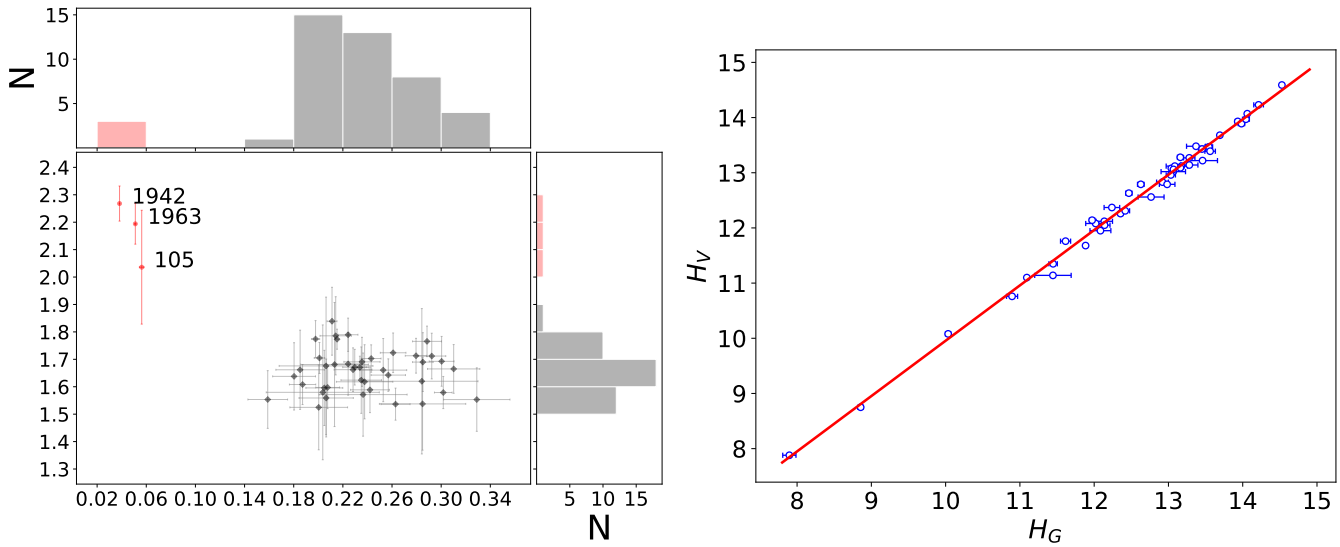

Figure 1. Left: The distributions of the G-band geometric albedo p_G and photometric slope $\beta_{\rm ref}$ for 44 asteroids. Right: The distribution of H_G vs. H_V for 44 asteroids. The red line represents the linear relationship $H_V = H_G$.

(63.°8 ± 1.°7, 74.°4 ± 1.°3) with a period of 3.0432333 ± 0.0000005 hr. Figure 4(c) in Appendix B shows example light curves for (8356) Wadhwa. The solution has a χ^2-value of 37.7 and an rms value of 0.0107 mag for Gaia data. The mirror pole of (251.°5, 89.°1) is rejected because of a larger rms value (0.0326 mag) for the Gaia data.

(23552) 1994 NB

Our work marks the first time that the physical parameters of (23552) 1994 NB are analyzed. For 1994 NB, we used 28 Gaia data points and six dense light curves observed in 2012 and 2023, published by P. A. Loera-González et al. (2023) and B. A. Skiff et al. (2023). In our analysis, we derived a pair of pole solutions with similar χ^2-values: (321.°0 ± 4.°6, −73.°2 ± 0.°9) and (164.°0 ± 2.°2, −83.°1 ± 0.°7). For the poles, similar rotation periods of about 3.628687 hr are derived. The corresponding χ^2-values are 8.7 and 9.6, and the rms values of the Gaia data are 0.0093 and 0.0139 mag, respectively. Accordingly, we could not indicate a preferred pole solution for the 1994 NB. Figure 4(d) in Appendix B shows example modeled light curves of 1994 NB for both pole solutions, indicating the solutions (321°, −73°) and (164°, −83°) with red and black symbols, respectively.

For all targets of this work, the input photometric data, derived model parameters, and figures of light curves fitting are available via the China-VO PaperData repository.[11] The spin parameters of 44 asteroids derived in this work are shown in Table 2, along with the corresponding values from the literature. Among our samples, 21 were previously reported of two or more possible pole orientations. After our analysis, the unique pole for 19 of them are derived. The rotation periods of 41 asteroids are consistent with previously reported values. For (587) Hypsipyle, we confirmed its rotation period as 2.8894654 hr which is different from the 13.6816 hr in J. Hanuš et al. (2016), but in agreement with the spin period given by J. Ďurech et al. (2020). Among the 44 asteroids, the pole solutions of 15 asteroids are close to the previous results. Meanwhile, some asteroids, such as (1942) Jablunka, (7055) Fabiopagan, and (56086) 1999 AA21, have different pole orientations from the previous results, particularly in pole ecliptic longitude.

[11] https://nadc.china-vo.org/res/r101597/

4.2. Phase Function Analysis

During photometric inversion, we also derived the absolute magnitudes H_G and photometric slopes $\beta_{\rm ref}$ of 44 asteroids in the Gaia G band; these are listed in Appendix B, Table 3. From the left panel of Figure 1, the values of $\beta_{\rm ref}$ for 41 asteroids are between 1.5 and 1.85, which correspond to S-complex class according to the results by J. Martikainen et al. (2021) and K. Muinonen et al. (2022). The three remaining asteroids, (105) Artemis, (1942) Jablunka, and (1963) Bezovec, have large values of $\beta_{\rm ref} > 2.0$, which implies C-complex class. These results support the hypothesis that S-complex asteroids predominate in the Phocaea region (J. M. Carvano et al. 2001). As for the three C-complex asteroids, asteroid (105) Artemis and (1963) Bezovec are classified into C-complex by spectral data and near-infrared color (S. J. Bus & R. P. Binzel 2002; D. J. Tholen 1984; M. Popescu et al. 2018). The asteroid (1942) Jablunka, with the color indices (g–r), (g–i), and (i–z) of 0.2988, 0.4040, and 0.0304 (A. V. Sergeyev et al. 2022), is also consistent with C-complex classification (F. DeMeo & B. Carry 2013). Actually, V. Carruba (2009) declare (105) Artemis as being an interloper of the Phocaea family. In our view, the asteroids (1942) Jablunka and (1963) Bezovec are not members of the Phocaea family either. Asteroid (1942) Jablunka of diameter of 16.7 km has been confirmed as the third largest member of the Tamara family (B. Novaković et al. 2017). Considering the large sizes of the asteroids (105) Artemis and (1963) Bezovec (94 km and 35 km, respectively) and the size of the parent of the Tamara family (106.1 km, estimated by B. Novaković et al. 2017), they cannot belong to the Tamara family.

The relation between the H_G magnitudes and the V-band absolute magnitudes H_V given by the Jet Propulsion Laboratory's service for the 44 asteroids is shown in the right panel of Figure 1. The high correlation coefficient of 0.9964 reflects the fact that the H_G values are consistent with the H_V system.

Using the derived G-band absolute magnitudes (H_G) and asteroid diameter (D) from the NEOWISE survey, we

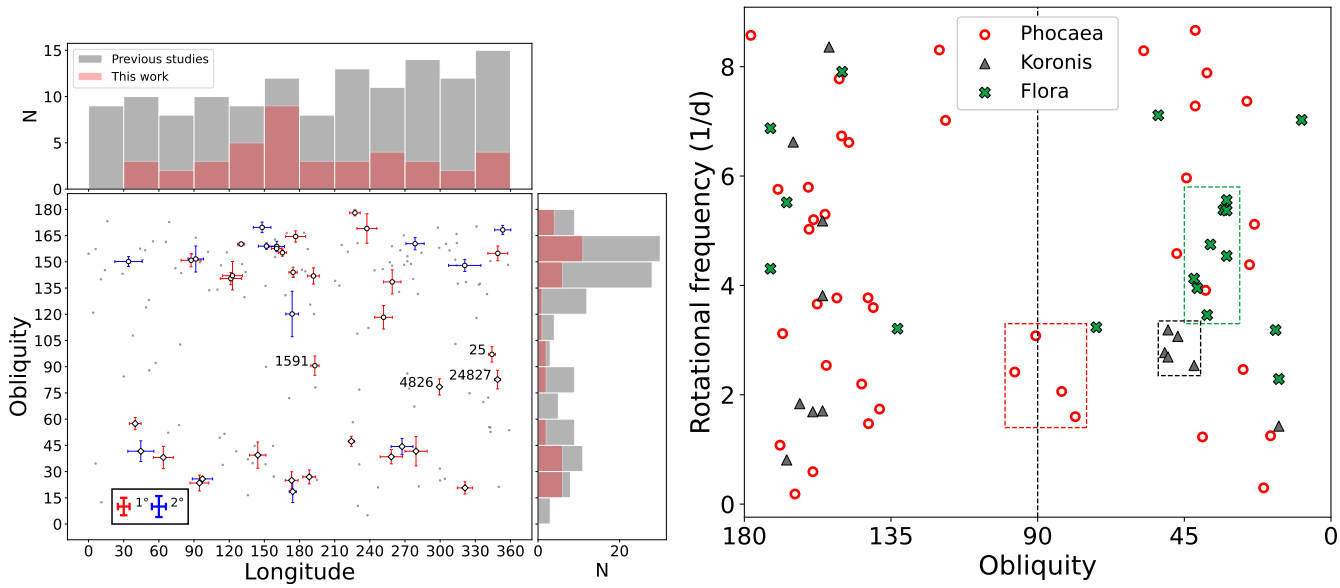

Figure 2. Left: The distributions of pole longitudes and obliquities for 172 asteroids (41 derived from our work and 131 from previous studies). Right: The distribution of obliquities vs. spin rates for the 41 asteroids.

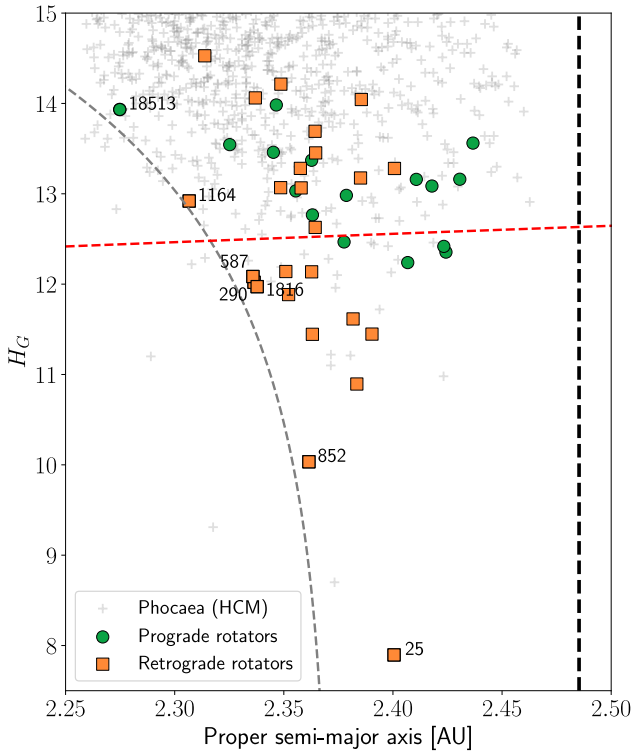

Figure 3. The distribution of the Phocaea family members in the (H,a) plane, our targets are marked with squares and circles for retrograde and prograde rotators, respectively. The gray line indicates the inner boundary of the V-shape of the Phocaea family, while the black dashed line represents the inner boundary of the 3:1 resonance with Jupiter.

estimated their geometric albedos (p_G) in the G band of the 44 asteroids by Equation (4), because the Gaia G band covers a larger portion of the incident solar spectrum (H. Pentikäinen et al. 2024),

$$\log p_G = 6.247 - 0.4H_G - 2\log D. \quad (4)$$

The estimated geometric albedos p_G are listed in the last column of Table 3 in Appendix A. The uncertainties of the geometric albedos are estimated based on the errors of H_G. For the 41 asteroids with slope parameters smaller than 1.85, as shown in the left panel of Figure 1, the geometric albedos p_G are between 0.158 and 0.328 with a mean value of 0.238, which is consistent with typical geometric albedos of S-complex asteroids. The geometric albedos of asteroid (105) Artemis, (1942) Jablunka, and (1963) Bezovec are 0.056, 0.038, and 0.051, respectively, which is consistent with the geometric albedos of C-complex asteroids. Thus, we believe that the previously described 41 asteroids are members of the Phocaea family.

4.3. Footprints of the Yarkovsky and YORP Effects

To investigate the footprints of the Yarkovsky and YORP effects on the Phocaea family, only the derived physical parameters of the 41 S-complex asteroids are used. First, we analyze the pole distribution of the asteroids, as shown in the left panel of Figure 2, and we find that these poles tend to concentrate onto two distinct clusters in obliquity (angle between the rotational pole orientation of an asteroid and the normal vector of its orbital plane). The prograde cluster contains asteroids with obliquities ranging from 0° to 45°, and the retrograde cluster consists of asteroids with obliquities between 135° and 170°. Additionally, the four asteroids (25) Phocaea, (1591) Baize, (4826) Wilhelms, and (24827) Maryphil form a 'center group' around 90° in obliquity.

Besides the 41 S-complex asteroids in our analysis, we also searched members of unique pole solutions from previous studies, and find other 131 Phocaea family members (J. Hanuš et al. 2013a, 2013b, 2016, 2018, 2021; J. Ďurech et al. 2016, 2018, 2019, 2020; D. Hung et al. 2022; J. Ďurech & J. Hanuš 2023; A. Cellino et al. 2024), those data are shown as gray dots in the left panel of Figure 2. By comparison, pole longitudes from literature show more equilibrated, while the peak of retrograde is more significant than our samples. The ratios of prograde and retrograde rotators for whole data set and our samples are 60:112 and 15:26, respectively.

Table 1
Information on the Rates of Orbital Drift ($(da/dt)_{\rm orb}$), Asteroid Diameters (D), Bond Albedo (A), Obliquity (γ), Bulk Density (ρ), and Macroporosity (p) for Five Asteroids

Asteroid	$(da/dt)_{\rm orb}$ (10^{-4}/Myr)	D (km)	A	γ deg	ρ (g cm^{-3})	p (%)
290	-0.300 ± 0.029	9.82 ± 0.13	0.133 ± 0.025	138.5 ± 1.5	2.19 ± 0.23	41.2
587	-0.304 ± 0.030	11.02 ± 0.086	0.095 ± 0.022	120.2 ± 1.7	1.29 ± 0.15	65.4
852	-0.088 ± 0.008	26.54 ± 0.155	0.103 ± 0.006	158.8 ± 1.7	3.54 ± 0.36	4.8
1164	-0.551 ± 0.054	7.65 ± 0.064	0.091 ± 0.011	160.4 ± 2.2	1.97 ± 0.20	47.1
1816	-0.288 ± 0.028	9.78 ± 0.371	0.126 ± 0.008	150.9 ± 1.6	2.64 ± 0.28	29.2

The bimodal distribution of the obliquity with two peaks around 32° and 155° reflects the evidence of the long-term YORP effect on the pole orientation of the asteroids. This is consistent with the theoretical predictions (W. F. Bottke et al. 2006; P. Paolicchi & Z. Kneževicć 2016; D. Vokrouhlický et al. 2015) that obliquities of family members are changed toward extreme values 0° and 180° driven by the YORP effect. We conclude that the deviation of the two peaks from the theoretical extrema of 0° and 180° reflects the fact that pole reorientation is efficient near the theoretical extrema. In the analysis of the YORP effect for the Koronis members, S. M. Slivan (2002) first suggested the existence of the so-called Slivan states, the alignment of spin vectors and correlation of spin rates. A. Kryszczyńska (2013) also claimed that several members in the Flora family stayed in the Slivan state. As a comparison, we display the obliquities versus spin rates of 41 Phocaea family members with red symbols, Koronis members with black symbols, and Flora members with green symbols in the right panel of Figure 2. For the Koronis and Flora families, spin rates for the prograde rotators show a more significant cluster feature than that for the retrograde rotators. For the case of the Phocaea members, neither the prograde nor the retrograde rotators show a significant cluster trend in the spin rate distribution, whereas, the "center group" shows a significant cluster with spin rates ranging from 1.6 to 3.1 cycles/day.

Figure 3 shows a V-shape distribution of the H_G magnitude versus semimajor axis (a) of the Phocaea family members (gray pluses for all members, circles and squares symbols for the 41 analyzed targets in this work). Theoretical studies (D. Vokrouhlický et al. 2006, 2015; P. Paolicchi & Z. Kneževicć 2016) show that the formation of the V shape is due to the combined influence of the Yarkovsky and YORP effects. Since the family was formed by a collisional event, the Yarkovsky effect drives the prograde and retrograde fragments outward and inward, respectively. The smaller members of the family tend to move farther away from the parent body, resulting in such a V shape in the (H_G, a) space over millions of years. Based on the V shape of the Phocaea family, A. Milani et al. (2017) estimated its age of 1187 ± 319 Myr by using the inner boundary of the V shape. The fuzzy outer boundary of the Phocaea family (see Figure 3) is due to the effect of the 3:1 resonance with Jupiter. In the V-shape plot, the prograde and retrograde rotators are distinguished by orange and green colors, respectively. For our samples below the red line ($H_G = 12.4$ mag, $D = 8.8$ km assuming $p_G = 0.25$), retrograde rotators are strictly in the left part of the V shape and the prograde ones in the right part. For our samples above the red line, they mix to some extent. This mixture phenomenon could be the result of the YORP cycle. This refers to a timescale where the pole obliquity of an asteroid decreases or increases to 0° or 180°, respectively, due to the YORP effect, whereafter the pole of the asteroid tends to be reoriented randomly. Roughly, the YORP cycle is proportional to the sizes and heliocentric distances of the asteroids. Here, according to the method by P. Paolicchi & Z. Kneževicć (2016) and considering the Phocaea family age to be equal to the YORP cycle, we computed the H-threshold of the YORP cycle (drawn as the red dashed line in the V-shape plot). Consequently, those samples located above the red line should have undergone at least one YORP cycle, and their poles may have been reoriented randomly. By the YORP cycle, we can comprehend why the prograde asteroid (18513) 1996 TS5 occurs near the inner boundary of the V shape.

4.4. Estimation of Asteroid Densities

The age of an asteroid family is a key to understanding its origin and evolution. Considering certain evolutionary mechanisms, several different methods have been developed to determine the age of asteroid families. For collisional families, like the Phocaea family, the methods based on the Yarkovsky and YORP chronology (i.e., D. Nesvorný et al. (2003), D. Vokrouhlický et al. (2006), F. Spoto et al. (2015), W. F. Bottke et al. (2015)) are considered to be the most precise ones at present.

F. Spoto et al. (2015) determine the age of asteroid families based on the values of the slope of the V shape derived by iterative least-squares fitting with interloper removal. The inverse slope is Δa, the accumulated change in orbital semimajor a over the family age with unit $1/D$. Accordingly, the Yarkovsky drift rate da/dt for family members near the inner and outer boundaries of the V shape may be estimated by assuming that they keep moving inward or outward since the formation of the family.

Among the 41 Phocaea family asteroids, we choose five targets, the asteroids (290) Bruna, (587) Hypsipyle, (852) Wladilena, (1164) Kobolda, and (1816) Liberia close to the inner boundary, for the calculation of their Δa. As for the asteroid (18513) 1996 TS5, we do not include the asteroid (18513) 1996 TS5 in the sample, because of the complication of the drift by the YORP cycle. In order to determine the accumulated semimajor axis change, we estimate the center of the V shape of the Phocaea family (a_c) as 2.372 au by using the *dw*-method, a border technique for V-shape identification (M. Delbo et al. 2017, 2019) by fixing the slope value of the inner borders of the V shape given by A. Milani et al. (2017). With the estimated a_c and family age ($\tau_{\rm age}$), the approximation of the drift rates for the semimajor axis $(da/dt)_{\rm orb}$ for the five asteroids are calculated by $\Delta a/\tau_{\rm age}$. Considering that their migration in the orbital semimajor axis has risen from the Yarkovsky effect, we figure out their densities due to the

successful determination of their physical parameters, especially the Bond albedo (A) and pole obliquity (γ). For the goal, we use the Equation (5) in F. Spoto et al. (2015):

$$\frac{da}{dt} = \left(\frac{da}{dt}\right)_{\rm Bennu} \frac{\sqrt{a_{\rm Bennu}}}{\sqrt{a}} \frac{1-e^2_{\rm Bennu}}{1-e^2} \frac{D_{\rm Bennu}}{D} \times \frac{\rho_{\rm Bennu}}{\rho} \frac{\cos(\gamma)}{\cos(\gamma_{\rm Bennu})} \frac{1-A}{1-A_{\rm Bennu}}, \quad (5)$$

where D is the diameter of the asteroid retrieved from the NEOWISE survey, γ is the derived pole obliquity, ρ is the bulk density, and A is the Bond albedo computed from the geometric albedo $p_{_G}$ and the parameters G_1, G_2 of the H, G_1, G_2 photometric function. The subscript "Bennu" means the corresponding parameters of asteroid (101955) Bennu. The measured Yarkovsky drift rate $(da/dt)_{\rm Bennu}$ from the paper of D. Farnocchia et al. (2021) and the involved parameters of Bennu come from M. C. Nolan et al. (2013) and S. R. Chesley et al. (2014). The estimated densities of five asteroids (see the sixth column of Table 1) range from 1.29 to 3.54 g cm^{-3}. The uncertainty of $(da/dt)_{\rm orb}$ is estimated by a propagation of error considering the uncertainty of the family age. The uncertainty of bulk density was evaluated through 100,000 Monte Carlo simulations, taking into account the uncertainties in the $(da/dt)_{\rm orb}$, asteroid diameter, obliquity, and Bond albedo.

According to the spectroscopic data of the asteroids, the S-complex asteroids are linked to the ordinary chondrite meteorites (OCs). Compared to the densities of OCs, the density of asteroid (852) Wladilena is very close to that of the H chondrites, which is consistent with the result of J. W. Noonan et al. (2019), i.e., the core member (25) Phocaea is associated with H chondrites.

Using the average grain density of H chondrites $\rho_m = 3.72$ g cm^{-3}, the macroporosity of the five asteroids are calculated with the formula $P(\%) = 100(1 - \rho/\rho_m)$ (B. Carry 2012), as shown in Table 1. From the macroporosity values, the asteroids (290) Bruna, (587) Hypsipyle, and (1164) Kobolda have high macroporosities, indicating rubble-pile structures. Considering the shapes of (290) Bruna, (587) Hypsipyle, and (1164) Kobolda, we find them to resemble a 'top' shape (see Figure 5 in Appendix C).

5. Summary

(1) Combining dense and sparse photometric data obtained by ground-based and space-based telescopes, the physical parameters (including shape, spin parameters, and phase function parameters) of 44 asteroids in the Phocaea region are determined with the Bayesian light-curve inversion method.

(2) We derived the absolute Gaia magnitude H_G, the photometric slope $\beta_{\rm ref}$, and the geometric albedo in the G band $p_{_G}$ for the 44 asteroids. The estimated slopes and geometric albedos of 41 asteroids reflect the S-complex composition and that of three asteroids, (105) Artemis, (1942) Jablunka, and (1963) Bezovec, are C-complex. The three asteroids are probable interlopers for the Phocaea family, while (105) Artemis and (1963) Bezovec do not belong to members of the Tamara family, because of their significantly larger sizes.

(3) From the distribution of pole longitude λ_p versus pole obliquity γ of the 41 S-complex members, a bimodal distribution in γ is clear. The two existing clusters around the peak values of 32° and 155° are footprints of the long-term influence of the YORP effect on the Phocaea family. As for the spin rate of 41 asteroids, no significant Slivan state can be found among the prograde and retrograde clusters. Instead, four asteroids with obliquity around 90° have spin rates between 1.6 and 3.1 cycles/day.

(4) The distribution of the 41 asteroids in the V-shaped absolute magnitude versus semimajor axis (H_G,a) plot of the Phocaea family also show a significant footprint of the Yarkovsky effect. In agreement with the theoretical predictions, retrograde rotators tend to be left in the V shape and prograde rotators right except for a few samples. By using a threshold magnitude of $H_G = 12.4$ mag (equivalent to $D = 8.8$ km, assuming $p_{_G} = 0.25$) and the YORP cycle, the mixture of the prograde and retrograde rotators in the V-shape plot can be explained. The ratio of prograde to retrograde rotators is 0.57, which can be explained by the influence of the 3:1 mean motion resonance with Jupiter, due to which prograde asteroids tend to escape from the Phocaea region and may become sources of prograde rotating NEAs.

(5) By fitting the center position of the V shape and family age, we estimate the drift rates of the semimajor axis $(da/dt)_{\rm orb}$ for five asteroids with retrograde rotation very close to the inner boundary of the V shape. Assuming that the accumulated Δa derives from the Yarkovsky effect in the time of the family age, we estimate the densities of the five asteroids. Among the asteroids, (852) Wladilena has the highest density of 3.54 g cm^{-3}, which is very close to the bulk density of H chondrite meteorites. Besides asteroid (25) Phocaea, this is another member of H Chondrite material in Phocaea family. We think that the parent body of the Phocaea family has been composed of H chondrite-like material and the Phocaea family may be one of the sources of H chondrite meteorites. (587) Hypsipyle has the lowest bulk density of 1.29 g cm^{-3}, which is similar to that of asteroid Bennu (1.26 g cm^{-3}, estimated by S. R. Chesley et al. 2014). With the help of the grain density of H chondrites, we calculate the macroporosity of the five asteroids. The resulting macroporosity values of 41%, 65%, and 47% for (290) Bruna, (587) Hypsipyle, and (1164) Kobolda imply a rubble-pile structure. Their top-like shapes support this conclusion.

(6) Presently, a small number of 41 members of the Phocaea family are incorporated in the physical study of the family. Nevertheless, the footprints of the Yarkovsky and YORP effects in the Phocaea family can be clearly seen with the help of the members' physical parameters, i.e., their shapes, spin parameters, and phase function parameters. The future ground-based and space-based surveys will dramatically improve the knowledge of asteroid families. For example, the 10 year survey of the CSST will provide seven-band photometric data (apparent limiting magnitude of 26 mag in the G-band) and slitless spectra (wavelength range 225–1000 nm, apparent limiting magnitude of 23 mag) for faint members of high-inclination asteroid families, which can be used to determine the physical parameters of small family members. The present work marks the beginning of the physical studies of asteroid families by using incoming data gathered by from both space-based and ground-based surveys.

Acknowledgments

We are grateful to the referee for the useful suggestions and comments to the manuscript, which helped to improve its

contents. We would like to thank the financial support from the National Natural Science Foundation of China under grant No. 12288102 and the Yunnan Fundamental Research Project (grant No. 202305AS350009). This work is also supported by the National Natural Science Foundation of China (grant No. 12373069) and the Research Council of Finland (grants Nos. 359893 and 336546). We acknowledge the science research grants from the China Manned Space Project with Nos. CMS-CSST-2025-A16 ,CMS-CSST-2025-A18 and CMS-CSST-2025-A20, the Foreign Experts Project (FEP) State Administration of Foreign Experts Affairs of China (SAFEA) with No. G2021039001L and H20240864, and the Chinese Academy of Sciences President's International Fellowship Initiative (PIFI) grant No. 2021VMA0017.

This work uses data downloaded from the Asteroid Lightcurve Data Exchange Format (ALCDEF) database, which is supported by funding from the NASA grant 80NSSC18K0851. We also used data collected by the TESS mission funded by the NASA's Science Mission Directorate. This work has made use of data from the European Space Agency mission Gaia (https://www.cosmos.esa.int/gaia), processed by the Gaia Data Processing and Analysis Consortium (DPAC, https://www.cosmos.esa.int/web/gaia/dpac/consortium). Funding for the DPAC has been provided by national institutions, in particular the institutions participating in the Gaia Multilateral Agreement.

Appendix A
Physical Parameters of 44 Asteroids in the Phocaea Region

Table 2 summarizes the spin parameters of 44 asteroids determined in this work and the previous work.

Table 3 summarizes the phase function and related parameters of 44 asteroids determined in this work.

Table 2
Spin Parameters of 44 Asteroids in the Phocaea Region

Asteroid	Rotation Period				Pole Orientation (This Work)				Reference Pole				References
	P (hr)	σ_P (10^{-5} hr)	$P_{\rm ref}$ (hr)	$\sigma_{P,\rm ref}$ (10^{-5} hr)	λ_1 (°)	β_1 (°)	λ_2 (°)	β_2 (°)	λ_1 (°)	β_1 (°)	λ_2 (°)	β_2 (°)	
25	9.9354075	1.65	9.9354	1.0	344.2 ± 0.6	9.6 ± 0.9			347 ± 10	10 ± 10			(a)
105	37.1197492	3.86	37.118		44.7 ± 1.4	16.6 ± 1.4			47	24			(g)
			37.16	1000.0					233.5 ± 5	−42.5 ± 5			(h)
290	13.8055624	0.89	13.80554	1.0	259.1 ± 1.5	−70.1 ± 1.4			286 ± 10	−80 ± 10	37 ± 10	−74 ± 10	(a)
502	10.9266526	0.56	10.92666		174.5 ± 0.7	−41.3 ± 0.6			178 ± 6	−36 ± 5			(b)
			10.92666						184	−39	285	-45	(e)
587	2.8894654	0.39	2.889463	0.7	173.7 ± 1.8	−45.5 ± 4.8	323.4 ± 3.2	−31.6 ± 3.0	167 ± 4	−60 ± 4			(d)
			13.6816	50.0					232 ± 18	36 ± 15	55 ± 18	32 ± 15	(b)
852	4.6132965	0.08	4.613301	1.0	160.6 ± 2.2	−58.2 ± 0.7			181 ± 10	−48 ± 10	46 ± 10	−53 ± 10	(a)
			4.61334	1.0					170 ± 20	−57 ± 20			(f)
			4.6133						45	−53			(e)
1164	4.1417002	0.06	4.14168	2.0	278.6 ± 2.6	−53.3 ± 0.7			271 ± 9	−60 ± 3	6 ± 6	−54 ± 8	(d)
1192	6.5583613	0.02	6.55836		160.5 ± 0.9	−79.1 ± 0.3			133 ± 24	−78 ± 5	268 ± 16	−73 ± 5	(b)
			6.55836	1.0					144 ± 20	−66 ± 20			(f)
1568	6.6759829	0.29	6.67597		121.4 ± 1.8	−67.5 ± 0.7			109	-68			(i)
			6.67601						142	-75	279	-106	(e)
1591	7.7944596	0.69	7.79347	7.0	193.1 ± 0.7	23.7 ± 1.1			189 ± 1	45 ± 6	5 ± 2	−2 ± 4	(d)
1626	3.4201645	0.05	3.42015	0.7	251.7 ± 1.5	−43.2 ± 1.4			250 ± 3	−37 ± 4			(d)
			3.421367	0.3					152 ± 10	−9 ± 10			(j)
1816	3.0861619	0.10	3.086156		87.5 ± 1.7	−86.8 ± 0.8			73 ± 26	−68 ± 10			(b)
			3.086156	0.5					218 ± 20	−83 ± 20			(f)
1884	2.8944232	0.54	2.89442	2.0	39.8 ± 1.0	50.0 ± 0.7			42 ± 3	52 ± 3			(d)
1942	8.9116186	1.44	8.91158	1.0	187.0 ± 2.6	−79.6 ± 0.5			156 ± 15	−73 ± 15			(p)
			8.9115						220 ± 20	−55 ± 20			(f)
1963	18.1654180	0.71	18.1655	1.0	221.5 ± 0.6	1.4 ± 1.1			219 ± 10	7 ± 10			(a)
			18.1655	10.0					223 ± 20	−7 ± 20			(f)
			18.16539						222	2	73	−65	(e)
1987	9.4594916	0.12	9.4595	1.0	349.2 ± 1.7	−59.3 ± 0.8			352 ± 10	−58 ± 10			(a)
			9.4595	2.0					352 ± 10	−52 ± 10			(k)
2430	129.7460092	51.91	129.75	1000.0	176.7 ± 1.7	−68.2 ± 0.8			177 ± 5	−68 ± 5			(l)
2830	80.5771088	45.18	80.573	200.0	321.2 ± 1.3	44.0 ± 0.7			315 ± 5	34 ± 5			(m)
3388	3.2575139	0.14	3.25748	1.0	97.2 ± 2.9	82.4 ± 0.8			91 ± 20	82 ± 20			(f)
3895	3.5646214	0.04	3.56468	1.0	34.1 ± 3.9	−84.0 ± 1.0			33 ± 20	−74 ± 20	233 ± 20	−22 ± 20	(f)
			3.56462						49	-84	236	-15	(e)
			3.56461						349 ± 4	−86 ± 1			(d)
4132	3.2963327	0.08	3.29633	1.0	279.4 ± 1.9	71.2 ± 1.7			281	72			(a)
			3.296333						186	87			(c)
4742	5.4810471	0.55	5.48105	1.0	173.3 ± 1.1	45.3 ± 1.0			175 ± 20	37 ± 20			(f)
4826	15.0043414	0.82	15.0043		299.4 ± 0.3	1.7 ± 1.0			300 ± 3	3 ± 5			(d)
			15.00444						298	3			(e)
5040	4.6901545	0.11	4.690155	0.2	94.6 ± 1.6	42.7 ± 0.9			101 ± 10	48 ± 10			(n)
5325	4.0235788	0.12	4.02356	1.0	267.5 ± 3.1	65.7 ± 1.6			286 ± 15	73 ± 15			(o)
5647	6.1387299	0.87	6.1386		258.3 ± 1.9	64.0 ± 0.8			263 ± 20	51 ± 20			(f)
			6.13867	1.0					266	69			(a)
			6.13813						115	13			(e)
6510	6.3649158	0.36	6.3649	1.0	91.5 ± 2.2	−84.3 ± 2.6	273.2 ± 1.1	−79.3 ± 1.8	84 ± 15	−72 ± 15	249 ± 15	−37 ± 15	(p)

Table 2
(Continued)

Asteroid	Rotation Period				Pole Orientation (This Work)				Reference Pole				References
	P (hr)	σ_P (10^{-5} hr)	$P_{\rm ref}$ (hr)	$\sigma_{P,\rm ref}$ (10^{-5} hr)	λ_1 (°)	β_1 (°)	λ_2 (°)	β_2 (°)	λ_1 (°)	β_1 (°)	λ_2 (°)	β_2 (°)	
6522	7.6942197	0.84	7.69424		353.4 ± 2.3	−67.2 ± 0.4			353	−66			(c)
			7.6943	10.0					331 ± 20	−61 ± 20			(f)
6560	19.1980260	2.01	19.1981	10.0	174.2 ± 1.0	51.4 ± 2.3			174 ± 20	48 ± 20			(f)
7055	4.1687842	0.04	4.16879	1.0	148.1 ± 2.5	−62.4 ± 0.6			112 ± 20	−88 ± 20			(f)
8356	3.0432333	0.05			63.8 ± 1.7	74.4 ± 1.3							
8893	22.2785880	6.46	22.278	100.0	237.5 ± 1.7	−76.2 ± 1.8			225 ± 20	−78 ± 20			(f)
11271	6.3616731	1.19	6.36167	1.0	122.8 ± 1.7	−42.6 ± 1.8			104	−29	260	−29	(c)
15779	19.5284442	6.60	19.5268	10.0	144.4 ± 1.4	38.1 ± 1.6			157 ± 20	51 ± 20			(f)
18513	9.7459095	0.42	9.7458	10.0	188.3 ± 1.1	41.6 ± 0.8			194 ± 20	38 ± 20			(f)
22275	40.4764058	6.54	40.478	100.0	151.8 ± 2.3	−81.1 ± 0.9			127 ± 20	−76 ± 20			(f)
23200	16.3061677	0.85	16.3061	10.0	191.9 ± 1.0	−50.4 ± 1.1			199 ± 20	−56 ± 20			(f)
23552	3.6286870	0.09			321.0 ± 4.6	−73.2 ± 0.9	164.0 ± 2.2	−83.1 ± 0.7					
24827	11.6481124	0.80	11.6484	50.0	349.0 ± 0.5	24.6 ± 1.1			354 ± 7	12 ± 16			(d)
29032	5.2372338	0.15	5.23725	1.0	224.3 ± 0.5	28.5 ± 0.6			228 ± 20	41 ± 20			(f)
29729	4.5279868	0.11	4.52796	1.0	165.4 ± 0.7	−89.1 ± 0.6	343.5 ± 0.4	−85.6 ± 0.9	165 ± 20	−89 ± 20			(f)
32036	4.7746088	0.37	4.7746	10.0	130.2 ± 0.6	−83.7 ± 0.6			111 ± 20	−84 ± 20			(f)
54443	2.7993770	0.14	2.79937	1.0	227.3 ± 0.9	−66.3 ± 0.2			222 ± 20	−65 ± 20			(f)
56086	2.7701508	0.17	2.77018	1.0	44.6 ± 3.7	71.5 ± 2.0			13 ± 20	84 ± 20			(f)

References: (a) J. Hanuš et al. (2013b); (b) J. Hanuš et al. (2016); (c) J. Ďurech et al. (2019); (d) J. Ďurech et al. (2020); (e) D. Hung et al. (2022); (f) J. Ďurech & J. Hanuš (2023); (g) J. Hanuš et al. (2021); (h) S. Higley et al. (2008); (i) J. Hanuš et al. (2011); (j) R. D. Stephens & B. D. Warner (2021); (k) J. Hanuš et al. (2018); (l) J. Hanuš et al. (2013a); (m) J. Ďurech et al. (2018); (n) R. D. Stephens et al. (2021); (o) M. Husárik (2016); (p) J. Ďurech et al. (2016).

Table 3
Phase Function Parameters and Related Parameters of 44 Asteroids in the Phocaea Region

Asteroid	H_G	G_1	G_2	q	$\beta_{\rm ref}$	D	p_G
25	7.90 ± 0.09	0.27 ± 0.09	0.43 ± 0.10	0.47 ± 0.04	1.55 ± 0.12	61.05 ± 2.46	0.33 ± 0.03
105	8.86 ± 0.04	0.80 ± 0.21	0.06 ± 0.14	0.38 ± 0.02	2.04 ± 0.21	94.86 ± 23.22	0.06 ± 0.00
290	12.02 ± 0.13	0.37 ± 0.14	0.38 ± 0.15	0.47 ± 0.07	1.54 ± 0.17	9.82 ± 0.13	0.28 ± 0.04
502	10.89 ± 0.07	0.39 ± 0.06	0.34 ± 0.07	0.45 ± 0.04	1.66 ± 0.09	15.80 ± 1.16	0.31 ± 0.02
587	12.08 ± 0.14	0.39 ± 0.21	0.34 ± 0.20	0.45 ± 0.08	1.68 ± 0.23	11.02 ± 0.09	0.21 ± 0.03
852	10.03 ± 0.04	0.43 ± 0.03	0.30 ± 0.04	0.43 ± 0.02	1.70 ± 0.05	26.54 ± 0.15	0.24 ± 0.01
1164	12.92 ± 0.08	0.36 ± 0.13	0.35 ± 0.11	0.44 ± 0.04	1.60 ± 0.14	7.65 ± 0.06	0.20 ± 0.02
1192	12.63 ± 0.04	0.50 ± 0.03	0.26 ± 0.04	0.42 ± 0.02	1.77 ± 0.06	7.38 ± 0.19	0.29 ± 0.01
1568	11.88 ± 0.02	0.49 ± 0.06	0.24 ± 0.05	0.41 ± 0.01	1.70 ± 0.06	12.45 ± 0.08	0.20 ± 0.00
1591	11.45 ± 0.06	0.42 ± 0.10	0.31 ± 0.08	0.43 ± 0.03	1.68 ± 0.11	14.41 ± 0.24	0.22 ± 0.01
1626	11.44 ± 0.25	0.30 ± 0.22	0.46 ± 0.28	0.51 ± 0.14	1.58 ± 0.25	15.14 ± 0.49	0.20 ± 0.05
1816	11.97 ± 0.04	0.44 ± 0.08	0.29 ± 0.07	0.42 ± 0.02	1.69 ± 0.09	9.78 ± 0.37	0.30 ± 0.01
1884	12.35 ± 0.03	0.38 ± 0.10	0.32 ± 0.07	0.43 ± 0.02	1.69 ± 0.11	8.42 ± 0.39	0.29 ± 0.01
1942	13.04 ± 0.01	0.96 ± 0.07	−0.06 ± 0.05	0.35 ± 0.02	2.27 ± 0.06	16.77 ± 0.09	0.04 ± 0.00
1963	11.09 ± 0.01	0.88 ± 0.07	−0.01 ± 0.04	0.36 ± 0.01	2.19 ± 0.07	35.54 ± 0.23	0.05 ± 0.00
1987	11.61 ± 0.07	0.39 ± 0.06	0.33 ± 0.07	0.44 ± 0.03	1.69 ± 0.09	13.02 ± 0.16	0.24 ± 0.01
2430	12.14 ± 0.11	0.32 ± 0.08	0.46 ± 0.12	0.51 ± 0.06	1.55 ± 0.11	12.47 ± 0.32	0.16 ± 0.02
2830	12.47 ± 0.04	0.41 ± 0.07	0.30 ± 0.06	0.42 ± 0.02	1.71 ± 0.08	7.89 ± 0.10	0.29 ± 0.01
3388	13.37 ± 0.13	0.27 ± 0.12	0.45 ± 0.14	0.48 ± 0.07	1.52 ± 0.15	6.29 ± 0.31	0.20 ± 0.02
3895	12.14 ± 0.07	0.41 ± 0.05	0.34 ± 0.07	0.45 ± 0.03	1.66 ± 0.08	10.38 ± 0.09	0.23 ± 0.02
4132	12.24 ± 0.10	0.34 ± 0.11	0.38 ± 0.11	0.45 ± 0.05	1.62 ± 0.14	9.72 ± 0.06	0.24 ± 0.02
4742	13.16 ± 0.04	0.56 ± 0.06	0.20 ± 0.05	0.40 ± 0.02	1.79 ± 0.06	6.55 ± 0.14	0.22 ± 0.01
4826	12.98 ± 0.10	0.43 ± 0.09	0.31 ± 0.11	0.44 ± 0.05	1.64 ± 0.12	7.93 ± 0.12	0.18 ± 0.02
5040	13.09 ± 0.12	0.32 ± 0.13	0.42 ± 0.14	0.48 ± 0.06	1.56 ± 0.14	7.06 ± 0.00	0.21 ± 0.02
5325	12.77 ± 0.17	0.35 ± 0.25	0.40 ± 0.25	0.48 ± 0.11	1.62 ± 0.27	6.97 ± 0.23	0.28 ± 0.05
5647	12.42 ± 0.06	0.36 ± 0.04	0.34 ± 0.04	0.43 ± 0.02	1.64 ± 0.06	8.61 ± 0.23	0.26 ± 0.01
6510	13.07 ± 0.16	0.33 ± 0.11	0.43 ± 0.16	0.49 ± 0.08	1.57 ± 0.15	6.66 ± 0.09	0.24 ± 0.04
6522	13.17 ± 0.08	0.42 ± 0.08	0.33 ± 0.09	0.45 ± 0.04	1.66 ± 0.12	6.12 ± 0.12	0.25 ± 0.02
6560	13.03 ± 0.06	0.37 ± 0.05	0.39 ± 0.06	0.47 ± 0.03	1.61 ± 0.07	7.60 ± 0.00	0.19 ± 0.01
7055	13.07 ± 0.03	0.41 ± 0.02	0.33 ± 0.03	0.44 ± 0.02	1.67 ± 0.04	6.69 ± 0.65	0.23 ± 0.01
8356	13.16 ± 0.02	0.56 ± 0.11	0.20 ± 0.07	0.40 ± 0.02	1.84 ± 0.12	6.75 ± 0.31	0.21 ± 0.00
8893	14.21 ± 0.06	0.52 ± 0.12	0.24 ± 0.10	0.41 ± 0.03	1.79 ± 0.14	4.12 ± 0.08	0.21 ± 0.01
11271	13.28 ± 0.12	0.43 ± 0.11	0.34 ± 0.12	0.45 ± 0.06	1.66 ± 0.14	6.82 ± 0.07	0.19 ± 0.02
15779	13.54 ± 0.05	0.38 ± 0.06	0.33 ± 0.06	0.43 ± 0.03	1.60 ± 0.08	5.70 ± 0.10	0.21 ± 0.01
18513	13.93 ± 0.03	0.42 ± 0.05	0.29 ± 0.04	0.42 ± 0.02	1.71 ± 0.06	4.11 ± 0.69	0.28 ± 0.01
22275	13.28 ± 0.08	0.37 ± 0.10	0.34 ± 0.10	0.44 ± 0.04	1.62 ± 0.12	6.05 ± 0.01	0.23 ± 0.02
23200	13.45 ± 0.05	0.32 ± 0.05	0.40 ± 0.05	0.46 ± 0.03	1.54 ± 0.06	5.29 ± 1.17	0.26 ± 0.01
23552	13.69 ± 0.02	0.46 ± 0.06	0.26 ± 0.04	0.40 ± 0.01	1.77 ± 0.07	5.46 ± 0.00	0.20 ± 0.00
24827	13.46 ± 0.20	0.42 ± 0.21	0.37 ± 0.24	0.48 ± 0.11	1.68 ± 0.25	5.95 ± 0.35	0.21 ± 0.04
29032	13.98 ± 0.04	0.50 ± 0.05	0.25 ± 0.05	0.41 ± 0.02	1.72 ± 0.07	4.16 ± 0.05	0.26 ± 0.01
29729	14.04 ± 0.05	0.40 ± 0.06	0.32 ± 0.06	0.43 ± 0.03	1.67 ± 0.07	4.31 ± 0.03	0.23 ± 0.01
32036	14.53 ± 0.01	0.44 ± 0.04	0.27 ± 0.02	0.41 ± 0.01	1.77 ± 0.04	3.56 ± 0.53	0.22 ± 0.00
54443	14.06 ± 0.03	0.31 ± 0.03	0.41 ± 0.03	0.47 ± 0.01	1.58 ± 0.06	3.73 ± 0.19	0.30 ± 0.01
56086	13.56 ± 0.07	0.29 ± 0.06	0.42 ± 0.07	0.47 ± 0.03	1.59 ± 0.08	5.24 ± 0.09	0.24 ± 0.02

Appendix B
Example Asteroids for Light-curve Inversion

Here, we present the dense light curves and Gaia photometric data of four example asteroids in Figure 4. The blue circles represent the observed data. The red and blue lines represent the model magnitudes computed for the pairs of pole solutions. For clarity, light curves are offset for the two pole solutions. The bottom scatter plots describe "observed-minus-computed" residuals for the observed and modeled photometric points, with red and black symbols representing the best-fit solution and its mirror solution, respectively.

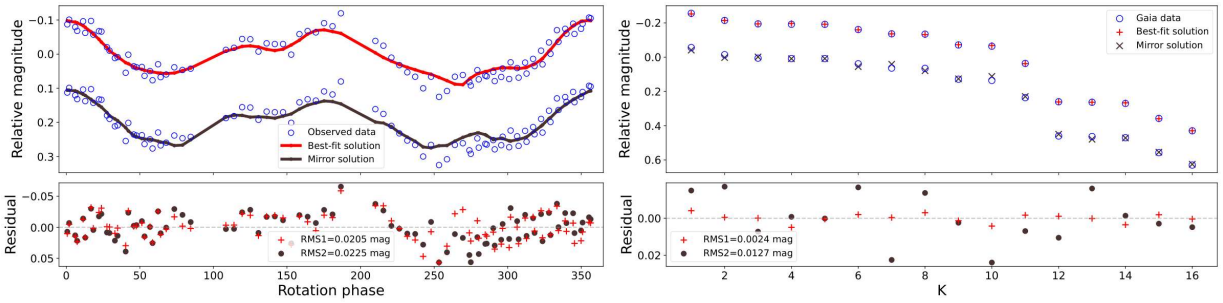

(a) Example ground-based photometric lightcurves #3 and the Gaia lightcurves for asteroid (1626) Sadeya.

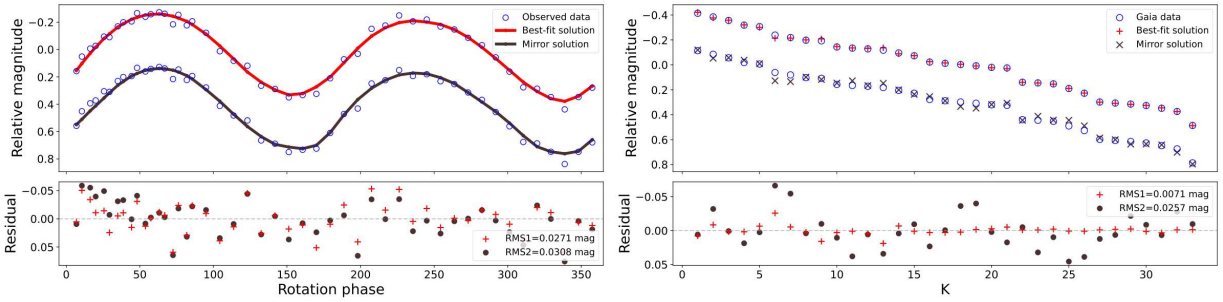

(b) Example TESS photometric lightcurves #9 and the Gaia lightcurves for asteroid (6560) Pravdo.

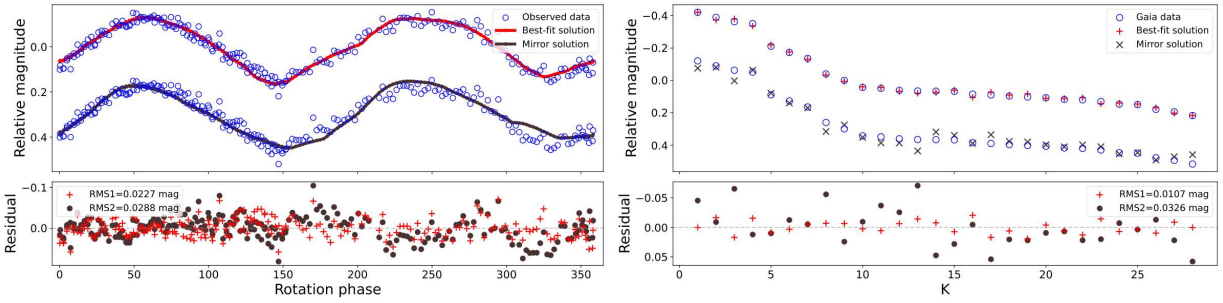

(c) Example ground-based photometric lightcurves #10 and the Gaia lightcurves for asteroid (8356) Wadhwa.

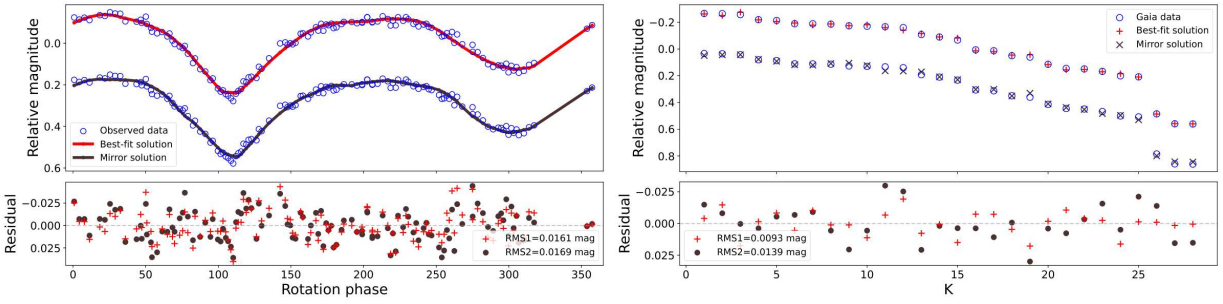

(d) Example ground-based photometric lightcurves #5 and the Gaia lightcurves for asteroid (23552) 1994 NB.

Figure 4. Example light curves of four example asteroids, where K is the number of Gaia photometric data points.

Appendix C
Convex Shapes

Figure 5 shows the convex shape of 44 asteroids corresponding to admissible pole solution, where the shapes of asteroids (587) Hypsipyle, (6510) Tarry, (23552) 1994 NB, and (29729) 1999 BY 1 correspond to the pole solutions (173°, −45°), (91°, -84°), (321°, −73°), and (343°, −85°), respectively.

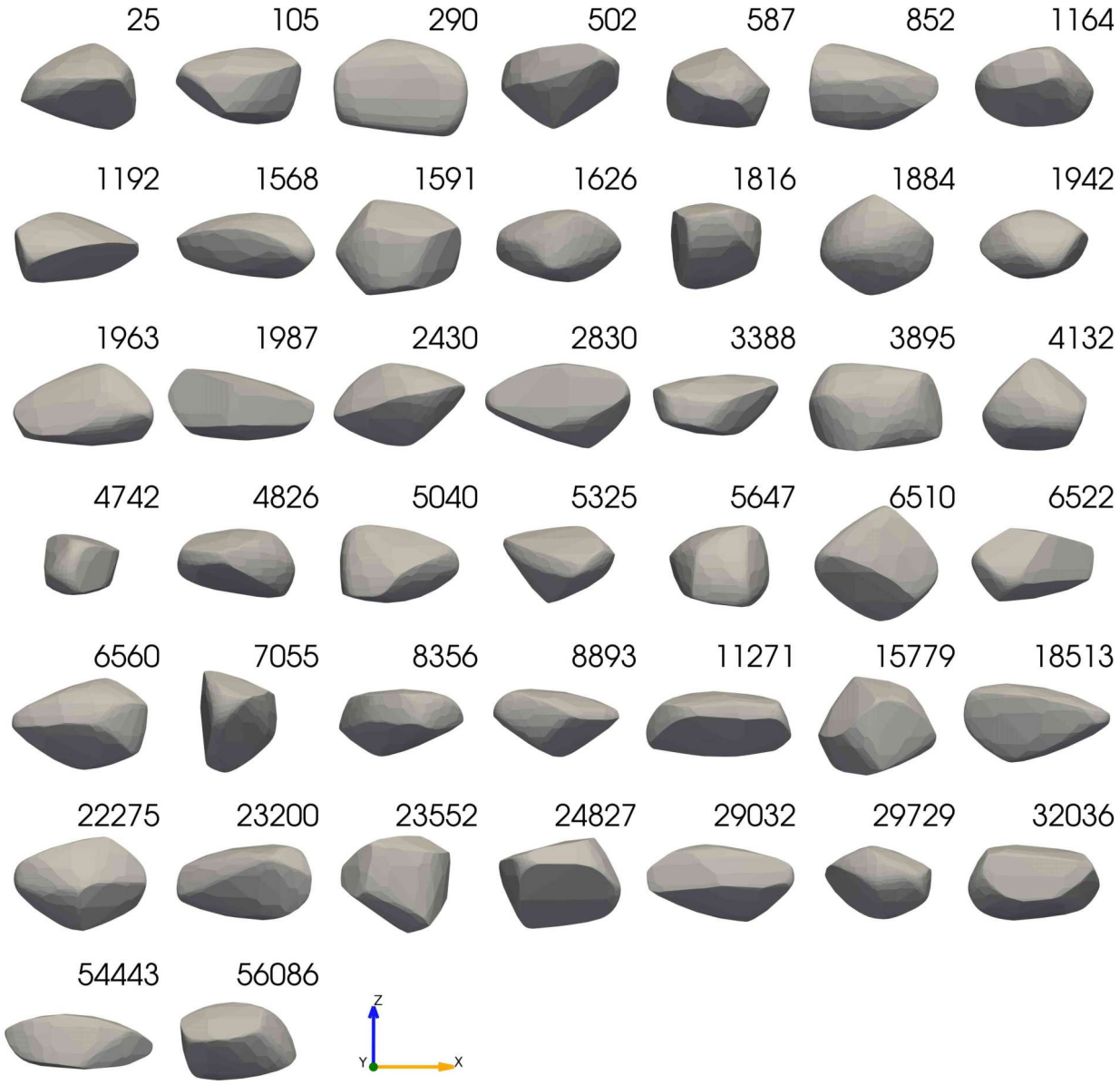

Figure 5. The convex shapes of 44 asteroids in the Phocaea region.

ORCID iDs

Xiaobing Wang https://orcid.org/0000-0002-7421-0532
Karri Muinonen https://orcid.org/0000-0001-8058-2642
Antti Penttilä https://orcid.org/0000-0001-7403-1721
Fukun Xu https://orcid.org/0000-0002-8618-3551

References

Bottke, W. F., Brož, M., & O'Brien, D. P. 2015, in Asteroids IV, ed. P. Michel, F. DeMeo, & W. Bottke (Tucson, AZ: Univ. Arizona Press), 701
Bottke, W. F., Jedicke, R., Morbidelli, A., Petit, J.-M., & Gladman, B. 2000, Sci, 288, 2190
Bottke, W. F., Vokrouhlický, D., Rubincam, D. P., & Nesvorný, D. 2006, AREPS, 34, 157
Buchheim, R. K. 2009, MPBu, 36, 84
Bus, S. J., & Binzel, R. P. 2002, Icar, 158, 146
Carruba, V. 2009, MNRAS, 398, 1512
Carry, B. 2012, P&SS, 73, 98
Carvano, J. M., Lazzaro, D., Mothé-Diniz, T., Angeli, C. A., & Florczak, M. 2001, Icar, 149, 173
Cellino, A., Tanga, P., Muinonen, K., & Mignard, F. 2024, A&A, 687, A277
Chesley, S. R., Farnocchia, D., Nolan, M. C., et al. 2014, Icar, 235, 5
Delbo, M., Avdellidou, C., & Morbidelli, A. 2019, A&A, 624, A69
Delbo, M., Walsh, K., Bolin, B., Avdellidou, C., & Morbidelli, A. 2017, Sci, 357, 1026
DeMeo, F., & Carry, B. 2013, Icar, 226, 723
Ďurech, J., & Hanuš, J. 2023, A&A, 675, A24
Ďurech, J., Hanuš, J., & Alí-Lagoa, V. 2018, A&A, 617, A57
Ďurech, J., Hanuš, J., Oszkiewicz, D., & Vančo, R. 2016, A&A, 587, A48
Ďurech, J., Hanuš, J., & Vančo, R. 2019, A&A, 631, A2
Durech, J., Sidorin, V., & Kaasalainen, M. 2010, A&A, 513, A46
Ďurech, J., Tonry, J., Erasmus, N., et al. 2020, A&A, 643, A59
Farnocchia, D., Chesley, S. R., Takahashi, Y., et al. 2021, Icar, 369, 114594
Granvik, M., Morbidelli, A., Jedicke, R., et al. 2018, Icar, 312, 181
Gu, S., Wang, X., Yeung, B., et al. 2022, AN, 343, e20224022
Hanuš, J., Brož, M., Durech, J., et al. 2013a, A&A, 559, A134
Hanuš, J., Delbo', M., Ďurech, J., & Alí-Lagoa, V. 2018, Icar, 309, 297
Hanuš, J., Ďurech, J., Brož, M., et al. 2011, A&A, 530, A134
Hanuš, J., Ďurech, J., Brož, M., et al. 2013b, A&A, 551, A67
Hanuš, J., Ďurech, J., Oszkiewicz, D. A., et al. 2016, A&A, 586, A108
Hanuš, J., Pejcha, O., Shappee, B. J., et al. 2021, A&A, 654, A48
Higley, S., Hardersen, P., & Dyvig, R. 2008, MPBu, 35, 63

Hung, D., Hanuš, J., Masiero, J. R., & Tholen, D. J. 2022, PSJ, 3, 56
Husárik, M. 2016, EM&P, 119, 35
Ivezic, Z., Juric, M., Lupton, R., et al. 2020, SDSS Moving Object Catalog V1.0, NASA Planetary Data System, doi:10.26033/bv8r-xe89
Kryszczyńska, A. 2013, A&A, 551, A102
Loera-González, P. A., Olguìn, L., Saucedo, J. C., et al. 2023, MPBu, 50, 258
Marsset, M., DeMeo, F. E., Burt, B., et al. 2022, AJ, 163, 165
Martikainen, J., Muinonen, K., Penttilï, A., Cellino, A., & Wang, X.-B. 2021, A&A, 649, A98
Masiero, J. R., DeMeo, F. E., Kasuga, T., & Parker, A. H. 2015, in Asteroids IV, ed. P. Michel, F. DeMeo, & W. Bottke (Tucson, AZ: Univ. Arizona Press), 323
Milani, A., Knežević, Z., Spoto, F., et al. 2017, Icar, 288, 240
Muinonen, K., Torppa, J., Wang, X.-B., Cellino, A., & Penttilä, A. 2020, A&A, 642, A138
Muinonen, K., Uvarova, E., Martikainen, J., et al. 2022, FrASS, 9, 1
Nesvorný, D., Bottke, W. F., Levison, H. F., & Dones, L. 2003, ApJ, 591, 486
Nolan, M. C., Magri, C., Howell, E. S., et al. 2013, Icar, 226, 629
Noonan, J. W., Reddy, V., Harris, W. M., et al. 2019, AJ, 158, 213
Novaković, B., Tsirvoulis, G., Granvik, M., & Todović, A. 2017, AJ, 153, 266
Novaković, B., Vokrouhlický, D., Spoto, F., & Nesvorný, D. 2022, CeMDA, 134, 34
Pál, A., Szakáts, R., Kiss, C., et al. 2020, ApJS, 247, 26
Paolicchi, P., & Kneževicć, Z. 2016, Icar, 274, 314
Pentikäinen, H., MacLennan, E., Uvarova, E., et al. 2024, in EPSC2024-894, 17 (Brussels: Europlanet Society),
Popescu, M., Licandro, J., Carvano, J. M., et al. 2018, A&A, 617, A12
Riello, M., De Angeli, F., Evans, D. W., et al. 2021, A&A, 649, A3
Sergeyev, A. V., Carry, B., Onken, C. A., et al. 2022, A&A, 658, A109
Skiff, B. A., McLelland, K. P., Sanborn, J. J., & Koehn, B. W. 2023, MPBu, 50, 74
Slivan, S. M. 2002, Natur, 419, 49
Spoto, F., Milani, A., & Knežević, Z. 2015, Icar, 257, 275
Stassun, K. G., Oelkers, R. J., Pepper, J., et al. 2018, AJ, 156, 102
Stephens, R. D., Coley, D. R., & Warner, B. D. 2021, MPBu, 48, 246
Stephens, R. D., & Warner, B. D. 2021, MPBu, 48, 56
Tanga, P., Pauwels, T., Mignard, F., et al. 2023, A&A, 674, A12
Tholen, D. J. 1984, PhD thesis, Univ. Arizona
Vokrouhlický, D., Bottke, W. F., Chesley, S. R., Scheeres, D. J., & Statler, T. S. 2015, in Asteroids IV, ed. P. Michel, F. DeMeo, & W. Bottke (Tucson, AZ: Univ. Arizona Press), 509
Vokrouhlický, D., Brož, M., Bottke, W., Nesvorný, D., & Morbidelli, A. 2006, Icar, 182, 118
Warner, B. D., Harris, A. W., & Pravec, P. 2009, Icar, 202, 134
Xu, X., Wang, X., Muinonen, K., et al. 2023, MNRAS, 521, 3925
Zhan, H. 2021, ChSBu, 66, 1290